Nano-Micro Letters

ISSN 2311-6706
e-ISSN 2150-5551
CN 31-2103/TB

ARTICLE

https://doi.org/10.1007/s40820-022-00795-8

Cite as
Nano-Micro Lett.
(2022) 14:48

Received: 3 November 2021
Accepted: 26 December 2021
Published online: 25 January 2022

Crystal Facet Engineering of TiO_2 Nanostructures for Enhancing Photoelectrochemical Water Splitting with $BiVO_4$ Nanodots

Mi Gyoung Lee[1], Jin Wook Yang[1], Hoonkee Park[1], Cheon Woo Moon[2], Dinsefa M. Andoshe[1], Jongseong Park[1], Chang-Ki Moon[1], Tae Hyung Lee[1], Kyoung Soon Choi[3], Woo Seok Cheon[1], Jang-Joo Kim[1], Ho Won Jang[1,4] ✉

HIGHLIGHTS

- Two types of $BiVO_4/TiO_2$ heterostructure photoanodes comprising TiO_2 nanorods (NRs) and TiO_2 nanoflowers (NFs) with different (001) and (110) crystal facets, respectively, were designed.
- The higher photoactivity of $BiVO_4/TiO_2$ NFs than $BiVO_4/TiO_2$ NRs was attributed to the improvement of charge separation by the TiO_2 NFs.
- The formation of type II band alignment between $BiVO_4$ nanodots and TiO_2 NFs expedited electron transport and reduced charge recombination.

ABSTRACT Although bismuth vanadate ($BiVO_4$) has been promising as photoanode material for photoelectrochemical water splitting, its charge recombination issue by short charge diffusion length has led to various studies about heterostructure photoanodes. As a hole blocking layer of $BiVO_4$, titanium dioxide (TiO_2) has been considered unsuitable because of its relatively positive valence band edge and low electrical conductivity. Herein, a crystal facet engineering of TiO_2 nanostructures is proposed to control band structures for the hole blocking layer of $BiVO_4$ nanodots. We design two types of TiO_2 nanostructures, which are nanorods (NRs) and nanoflowers (NFs) with different (001) and (110) crystal facets, respectively, and fabricate $BiVO_4/TiO_2$ heterostructure photoanodes. The $BiVO_4/TiO_2$ NFs showed 4.8 times higher photocurrent density than the $BiVO_4/TiO_2$ NRs. Transient decay time analysis and time-resolved photoluminescence reveal the enhancement is attributed to the reduced charge recombination, which is originated from the formation of type II band alignment between $BiVO_4$ nanodots and TiO_2 NFs. This work provides not only new insights into the interplay between crystal facets and band structures but also important steps for the design of highly efficient photoelectrodes.

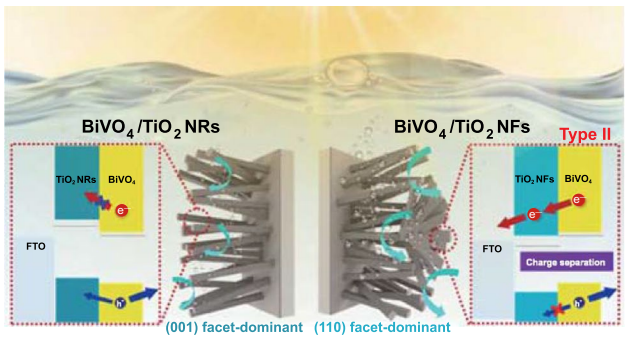

KEYWORDS Crystal facet control; Bismuth vanadate; Titanium dioxide; Heterojunction; Water splitting

Mi Gyoung Lee and Jin Wook Yang have contributed equally to this work.

✉ Ho Won Jang, hwjang@snu.ac.kr
[1] Department of Materials Science and Engineering, Research Institute of Advanced Materials, Seoul National University, Seoul 08826, Republic of Korea
[2] Department of Chemistry and Nanoscience, Ewha Womans University, Seoul 03693, Republic of Korea
[3] National Research Facilities and Equipment Center, Korea Basic Science Institute, Daejeon 34133, Republic of Korea
[4] Advanced Institute of Convergence Technology, Seoul National University, Suwon 16229, Republic of Korea

1 Introduction

Solar-driven photoelectrochemical (PEC) water splitting is considered a major breakthrough to settle an energy crisis. Despite its promise, the commercialization of PEC water splitting has been limited because of the relatively low efficiency and stability [1]. Although metal oxide-based photoelectrodes such as TiO_2, Fe_2O_3, WO_3, and $BiVO_4$ can be easily synthesized, major limitations such as charge recombination and short carrier lifetimes of from picosecond (*ps*) to nanosecond (*ns*) restrict their photoactivity.

The construction of heterostructure photoelectrodes is an effective approach to improve light absorption, carrier separation, and charge transfer efficiencies [2, 3]. Since it relies on the appropriate band alignment like type II heterojunction, the combination of photoelectrode materials having proper band edge positions is a key for determining their functionality in PEC water splitting. Among various heterostructures such as Fe_2O_3/WO_3 [4], $BiVO_4/WO_3$ [5–7], Fe_2O_3/SnO_2 [8–10], In_2S_3/In_2O_3 [11], and $BiVO_4/SnO_2$ [12, 13], $BiVO_4$-based heterostructure photoanodes have been widely studied since short charge diffusion lengths and lifetimes of $BiVO_4$ cause severe charge recombination. In a representative $BiVO_4/WO_3$ heterostructure, WO_3 enhances the charge separation as a hole blocking layer of $BiVO_4$, forming the type II band alignment. However, it has a relatively positive flat band potential of about 0.4 V versus (vs.) a reversible hydrogen electrode (RHE), which results in potential energy losses for electrons as they are transferred from the WO_3 to the $BiVO_4$, limiting the photovoltage of the combined system [5–7]. Also, the oxidation of surface hydroxyl groups of WO_3 causes the formation of peroxo-species, which reduces the stability of heterostructure photoanodes [13].

Compared to the WO_3, rutile TiO_2 is highly stable in a wide range of pH and has a relatively negative flat band potential of about 0.2 V versus RHE, which does not significantly limit the photovoltage obtainable from $BiVO_4$ [14–16]. However, TiO_2 has an intrinsic limitation of low electrical conductivity to be used as the hole blocking layer for $BiVO_4$ [17]. To resolve the problem, the increment of carrier concentration through doping and nanostructuring is required. In particular, both high surface area and electrical conductivity can be obtained by designing one-dimensional (1D) nanostructures such as nanorods (NRs), nanowires, and nanoflowers (NFs). Andoshe et al. developed S, N co-doped TiO_2 NRs and increased their carrier concentration and electrical conductivity [18]. The second problem is a mismatched band structure between $BiVO_4$ and TiO_2. A relatively positive valence band edge of TiO_2 makes it difficult to form the type II heterostructure suitable for charge separation. In order to utilize TiO_2 as the hole blocking layer for $BiVO_4$, the control of band edge position is necessary, and crystal facet engineering has emerged as an emerging strategy. According to the previous works, metal oxides provided various band edge positions depending on their crystal facets [19–21]. For instance, Wang et al. demonstrated that the (111) facet of Cu_2O, with a lower work function than the (100) facet, is unfavorable for the migration of holes from the Cu_2O surface to Pd through a semiconductor–metal junction [22]. It is reasonable to select and control the contact facet for the heterostructure to achieve suitable band structures and efficient charge separation.

In this work, we compare two types of $BiVO_4/TiO_2$ heterostructure photoanodes with different (001) and (110) crystal facets of TiO_2, which are NRs and NFs, respectively. After $BiVO_4$ nanodots are conformally electrodeposited on the surface of the TiO_2 nanostructures, the photocurrent density of $BiVO_4/TiO_2$ NFs increases by about 4.7 times, while that of $BiVO_4/TiO_2$ NRs decreases. Based on the analysis of charge carrier dynamics, it is revealed that the difference is derived by the charge separation ability of crystal facet-engineered TiO_2. The ultraviolet photoemission spectroscopy (UPS) represents band edge positions of TiO_2 nanostructures are significantly dependent on their crystal facet. Since TiO_2 NFs with (110) facets have relatively negative band edges, as a hole blocking layer they form type II heterojunction with $BiVO_4$ nanodots. In addition, the initial facet of TiO_2 has a decisive effect on the final architecture of the $BiVO_4/TiO_2$ due to the difference in the tendency of the $BiVO_4$ electrodeposition on the nanostructured TiO_2. In a word, crystal facet engineering plays a key role in affecting charge separation and in determining photoactivity. These findings provide a feasible avenue to adjust diverse metal oxides for use as photoelectrodes for desirable solar water splitting.

2 Experimental Section

2.1 Synthesis of TiO_2 NRs and TiO_2 NFs

TiO_2 NRs and TiO_2 NFs were grown on fluorine doped tin oxide (FTO) glass substrates using hydrothermal synthesis

 https://doi.org/10.1007/s40820-022-00795-8

similar to those in a previously reported paper [18]. Briefly, the precursor solution was prepared with 0.8 mL of titanium (IV) butoxide ($C_{16}H_{36}O_4Ti$, 97%, Aldrich), 5 mg of sulfamic acid (NH_2SO_3H, 99.3%, Aldrich), 25 mL of HCl (38%, Daejung), and 25 mL of deionized water (dH_2O) under magnetic stirring. After vigorous magnetic stirring for another 10 min, the solution was poured into Teflon vessel. The Teflon vessel, which contained the precursor solution and the FTO glass, was inserted into the autoclave and heated for 4 h at 180 °C in an oven and kept inside until the temperature reached room temperature. The synthesized TiO_2 NRs were removed from the Teflon vessel and rinsed repeatedly using dH_2O. After sufficient rinsing, the TiO_2 NRs were annealed at 500 °C for 3 h with 5% H_2/95% N_2 gas. For the synthesis of the TiO_2 NFs, a larger amount of sulfamic acid was added to the precursor solution, and the reaction time was increased over that of the TiO_2 NRs. A precursor solution for the growth of TiO_2 NFs was prepared with 100 mg of sulfamic acid (NH_2SO_3H, 99.3%, Aldrich), 0.8 mL of titanium butoxide ($C_{16}H_{36}O_4Ti$, 97%, Aldrich), and 50 mL of HCl solution (25 mL of dH_2O and 25 mL of concentrated HCl (38%, Daejung)). After vigorous stirring until the solution became completely clear, the solution was transferred to the Teflon vessel and moved into an autoclave. The autoclave was sealed and heated to the reaction temperature (180 °C) in an oven for 12 h and maintained until the autoclave was cooled to room temperature. The synthesized TiO_2 NFs were washed with dH_2O and annealed at 500 °C for 3 h under 5% H_2/95% N_2 gas.

2.2 Fabrication of $BiVO_4/TiO_2$ Heterostructure Photoanodes

$BiVO_4$ was electrodeposited onto the two types of TiO_2 nanostructures using previously reported methods [5, 23]. A precursor was prepared by dissolving bismuth nitrate pentahydrate (BiN_3O_9, 98%, Junsei) in a solution of vanadium oxide sulfate hydrate ($VOSO_4$, 99.99%, Aldrich) at pH < 0.5 with nitric acid (HNO_3, 67%, Junsei). Then, sodium acetate (CH_3COONa, 99%, Aldrich) was added, raising the pH to ~ 5.1, which was then adjusted to pH 4.7 using a few drops of concentrated HNO_3. This mildly acidic pH condition is necessary because, at pH values > 5, vanadium (IV) precipitates form in the solution. Pulsed anodic electrodeposition was conducted in a standard three-electrode system with a working electrode of nanostructured TiO_2, an Ag/AgCl reference electrode, and a platinum counter electrode. The electrodeposition was potentiostatically carried out at 1.95 V versus Ag/AgCl at 80 °C and annealed at 500 °C for 6 h in air at a heating rate of 2 °C per minute to crystallize.

2.3 PEC Measurements

The photocurrent versus potential curves with a scan rate of 10 mV s^{-1} and photocurrent versus time curves were recorded with a solar simulator with an AM 1.5 G filter. The light intensity of the solar simulator was calibrated to 1 sun (100 mW cm^{-2}). The incident photon-to-current conversion efficiency (IPCE) was measured at 1.23 V versus RHE. The electrochemical impedance spectroscopy (EIS) was conducted by applying 1.23 V versus RHE. The sweeping frequency ranged from 100 to 0.1 kHz, with an AC amplitude of 10 mV. The measured spectra were fitted using ZSimpWin software. The Mott-Schottky (M-S) plots were plotted by potential scan in AC condition with a frequency of 1 kHz with the light off. The Faradaic efficiency and gas evolution were calculated by the gas chromatography system (7890B, Agilent Technologies) in an air-tight cell at 1.23 V versus RHE.

2.4 Characterization

The morphologies of all photoanodes were characterized by field-emission scanning electron microscopy (FESEM, MERLIN Compact, ZEISS). High-resolution transmission electron microscopic (HR-TEM) images and elemental distributions were obtained with TEM (JEM-2100F, JEOL) equipped energy-dispersive spectroscope (EDS). X-ray diffraction (XRD, D8-Advance, Bruker) characterization was performed to confirm the crystalline phase of the TiO_2 NRs, TiO_2 NFs, and $BiVO_4/TiO_2$ NFs. The absorption spectra of the TiO_2 NRs, TiO_2 NFs, and $BiVO_4$ were measured by UV–Visible spectroscopy (V-770, JASCO). The band structures of the $BiVO_4/TiO_2$ NFs and $BiVO_4/TiO_2$ NRs were determined by analyzing the UPS (Ultra DLD) in advanced in-situ surface analysis system (AiSAS)). The time-resolved photoluminescence of TiO_2 NFs, TiO_2 NRs, $BiVO_4/TiO_2$ NFs, and $BiVO_4/TiO_2$ NRs was measured using

photoluminescence (PL, FlouTime 300, PicoQuant) with an excitation laser having a wavelength of 405 nm.

2.5 FDTD Simulation

The simulations were performed on the FDTD solutions program (Lumerical Solutions). The dielectric function of rutile TiO_2 was adopted from a prominent report [24], and FTO was considered as a perfect dielectric with a constant refractive index of 2.2 based on the analysis of previous literature [25]. The detailed simulation condition is displayed in Fig. S2. The mesh size was 5×5 nm^2.

3 Results and Discussion

3.1 Synthesis and FDTD Simulations of TiO_2 Nanostructures

To synthesize $BiVO_4/TiO_2$ nanostructures, we introduced an all-solution process comprising hydrothermal synthesis and electrodeposition, which is cost-effective and eco-friendly fabrication method for photoelectrode [26]. First, two types of TiO_2 nanostructures, which are TiO_2 NRs and TiO_2 NFs, were prepared by the one-step hydrothermal synthesis method. By controlling the reaction time, precursor concentration, and pH, the morphology and alignment of TiO_2 nanostructures were changed into NRs and NFs, as illustrated in Fig. 1a, b. TiO_2 NRs and NFs have rutile structures with different lattice plane intensities, i.e., (001) and (110), as shown in XRD analysis (Fig. 1c). In the case of TiO_2 NRs, TiO_2 preferentially grew to the (001) direction and it makes the vertically aligned 1D structures, as shown in Fig. 1d, whereas TiO_2 NFs showing the increased (110) direction peak in XRD have a tendency to grow laterally, as shown in Fig. 1e. The long reaction time of 10 h not only caused new heterogeneous nucleation at the tip of the nanorods, but also led to the growth of nanoflowers. As a result, the morphology of TiO_2 NFs formed on the TiO_2 NRs was implemented. Also, in the hydrothermal synthesis of TiO_2, acids, such as hydrochloric acid, sulfuric acid, sulfonic acid, and sulfamic acid, play highly important roles for the preferential growth as well as stabilization of the rutile phases [27]. We made a more acidic environment by adding sufficient sulfamic acid in order to induce the specific facet growth of nanoflowers. Based on the long reaction time and acidic environment, unlike previous reports for synthesizing the TiO_2 NFs, we enable to construct well-maintained rectangular shape of TiO_2 NFs without additional process [28, 29].

To compare the photoactivity according to the major facet of TiO_2 nanostructures, photocurrent density and IPCE of the TiO_2 NRs and NFs are measured, as shown in Figs. 1f and S1. Both photocurrent density and IPCE of the TiO_2 NRs were higher than those of the TiO_2 NFs. Since the (001) facet possesses the highest surface energy due to the coordinately unsaturated Ti and O atoms on (001) and very large Ti–O–Ti bond angles, the (001) facet of TiO_2 was more reactive than the other facets such as (110) and (101) [30]. And vertically aligned 1D TiO_2 NRs can make direct and ordered channels for electron transport and enhance light absorption. Furthermore, minority charge diffusion paths can be decoupled to different directions to enhance the photocharge collection efficiency [31].

To clearly understand light-harvesting capacity according to the TiO_2 crystal facets, we performed a finite-domain time-difference (FDTD) simulation, as shown in Fig. 1g–i. The electric field ($|E|$) distribution was calculated and visualized using the FDTD method to assist in understanding the light absorption mechanism. The model for the FDTD simulation is shown in Fig. S2. We considered vertical-, 30°-tilted, and 50°-tilted TiO_2 NRs by reflecting the SEM images (Fig. 1d, e). The results of the simulated absorption distribution along the z-axis acquired at light wavelengths of 350, 450, and 550 nm. The FDTD results clearly show strong absorption enhancement in the (001)-facet-dominant TiO_2 NRs compared to the (110)-facet-dominant TiO_2 NFs, especially at the wavelength of 450 nm, indicating that the (001) facet traps the incident light efficiently. As shown in Figs. S3, S4, the real configuration of TiO_2 NFs showed a similar tendency with a piece of TiO_2. These FDTD simulation results are closely related to the photoactivity of facet-controlled TiO_2 nanostructures in linear sweep voltammetry (LSV) (Fig. 1f).

3.2 Characterization and PEC performances of TiO_2 NRs and $BiVO_4/TiO_2$ NRs

Controlled facets affect not only the photocurrent density of TiO_2 nanostructures but also the electrodeposition trend of $BiVO_4$ on the TiO_2. First, we constructed heterostructure

 https://doi.org/10.1007/s40820-022-00795-8

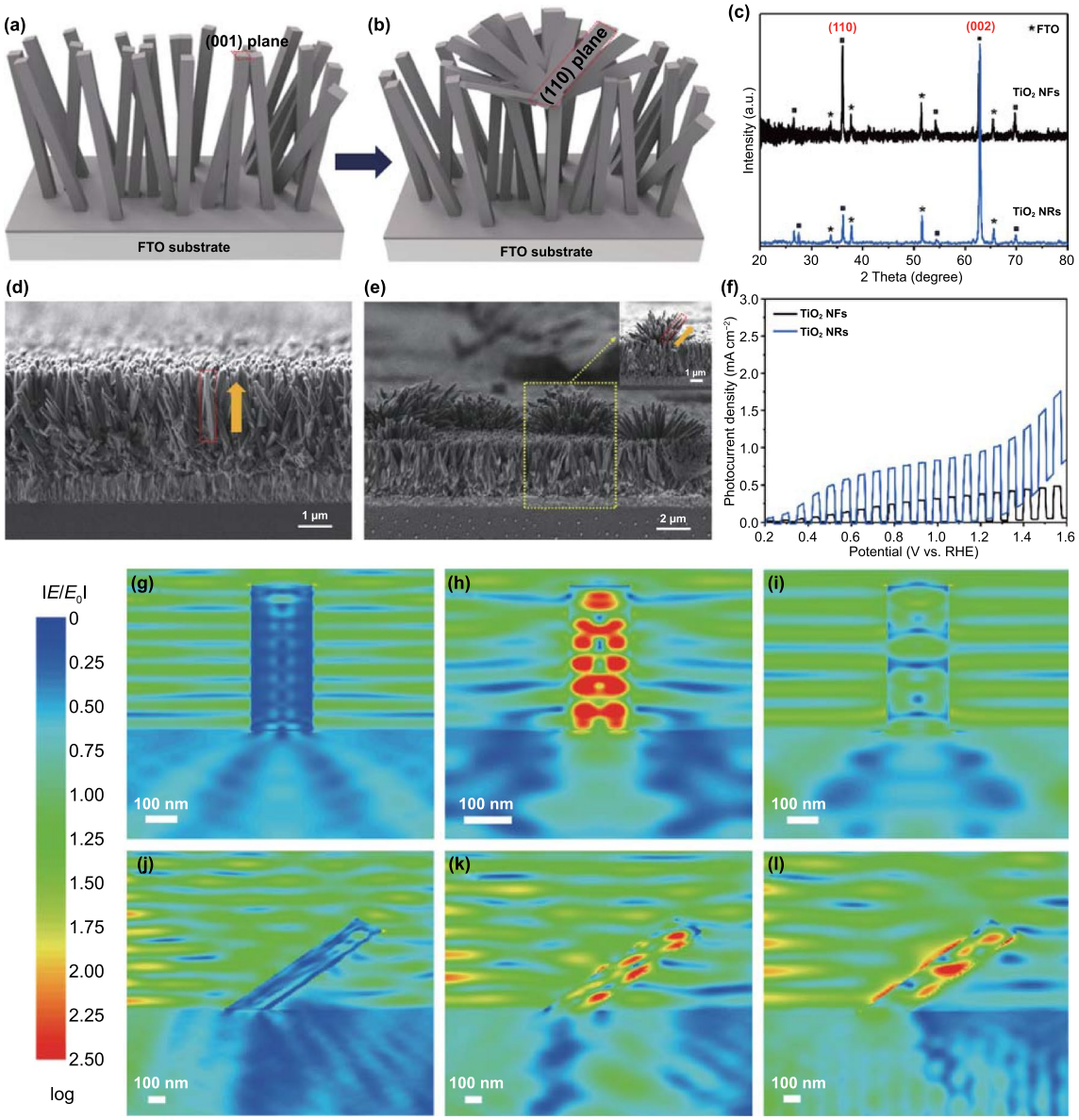

Fig. 1 Schematic illustration of **a** TiO_2 NRs and **b** TiO_2 NFs growth via hydrothermal synthesis. **c** XRD patterns of TiO_2 NRs and TiO_2 NFs. Cross-sectional SEM images of **d** TiO_2 NRs and **e** TiO_2 NFs. **f** *J*–*V* curves of TiO_2 NRs and TiO_2 NFs in 0.5M potassium phosphate ($K–P_i$) buffer with 1M Na_2SO_3. FDTD simulations of near field enhancement of TiO_2 NRs on FTO under **g** 350 nm, **h** 450 nm, and **i** 550 nm photons. FDTD simulations of near field enhancement of TiO_2 NFs on FTO under **j** 350 nm, **k** 450 nm, and **l** 550 nm photons

photoanodes of $BiVO_4/TiO_2$ NRs to demonstrate the effect of major facets of TiO_2 on the final architecture of $BiVO_4/TiO_2$ nanostructures and the following photoactivities. On the TiO_2 NRs, electrodeposited $BiVO_4$ nanodots agglomerate, and thus the tops of the $BiVO_4/TiO_2$ NRs are close to each other, as shown in Figs. 2a–c and S5. It is related to the concentration gradient in the solution under the electrodeposition process since ions tend to converge toward the vertex of TiO_2 NRs due to high conductivity. Agglomerated $BiVO_4$ nanodots block the gaps between the TiO_2 NRs, which might be deteriorating the light absorption and electrolyte permeation for PEC water splitting. As a result, the photocurrent

density of the $BiVO_4/TiO_2$ NRs (0.35 mA cm^{-2} at 1.23 V vs. RHE) was significantly less than that of pristine TiO_2 NRs (0.91 mA cm^{-2} at 1.23 V vs. RHE), as shown in Figs. 2d and S6. Also, as shown in Fig. S7, the IPCE of $BiVO_4/TiO_2$ NRs was significantly decreased to 22% under the wavelength of 390 nm at 1.23 V versus RHE, which means there are lots of charge recombination after the introduction of $BiVO_4$ on TiO_2 NRs.

We also analyzed the EIS to compare the charge transfer kinetics between the $BiVO_4/TiO_2$ NRs and TiO_2 NRs, as shown in Fig. 2e. Considering our architecture, we used the Haman equivalent circuit composed of three resistances and two capacitances since the EIS circuit is closely related to the structure of photoelectrodes [23]. In the EIS circuit, R_s is the series resistance, C_s and C_{ct} are the constant phase elements (CPE) for the semiconductor interface and the electrolyte/electrode interface, respectively, and R_{ct1} and R_{ct2} are the charge transfer resistances across the semiconductor interface and electrode/electrolyte interface, respectively. The values of R_s, R_{ct1}, and R_{ct2} obtained from the fittings are summarized in Table S1. The high photoactivity is represented by a small semicircle in the Nyquist plot. After the deposition of $BiVO_4$ nanodots, the charge transfer resistance across the electrode/electrolyte interface increased from 259.89 to 1948.06 Ω cm^2, showing the larger semicircles of $BiVO_4/TiO_2$ NRs compared to that of TiO_2 NRs. As shown in SEM images of $BiVO_4/TiO_2$ NRs (Fig. 2b, c), the agglomerated $BiVO_4$ reduced the porosity of the TiO_2 NRs, which is a structure interfering with the electrolyte permeation. Therefore, bulky $BiVO_4$ and reduced porosity of TiO_2 NRs become the main factors that increase the charge transfer resistance of $BiVO_4/TiO_2$ NRs photoanode. This result was also represented in that $BiVO_4/TiO_2$ NRs have a lower charge injection efficiency than TiO_2 NRs (Fig. 2f), which led to the deterioration of the PEC performances.

3.3 Characterization and PEC Performances of TiO_2 NFs and $BiVO_4/TiO_2$ NFs

In order to investigate differences in nanostructures and photoactivities according to the crystal facet, we set up TiO_2 NFs with (110) facets as a bottom layer for $BiVO_4$ nanodots. Unlike on the TiO_2 NRs, the conformal coating of extremely thin $BiVO_4$ nanodots across the entire surface of the TiO_2 NFs could be possible through the control of pulse cycles during the electrodeposition, as shown in Fig. S8. According to SEM images in Fig. 3a–d, the surfaces of TiO_2 NFs were totally covered with $BiVO_4$ nanodots by increasing the pulse cycles of $BiVO_4$. A cross-sectional SEM image in

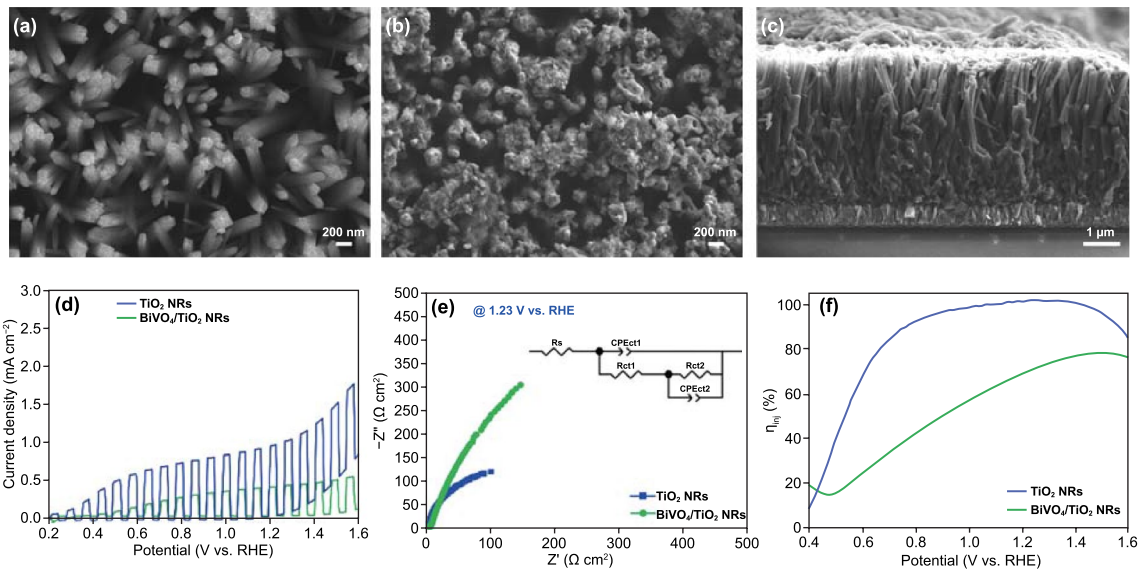

Fig. 2 Top SEM images of **a** TiO_2 NRs and **b** $BiVO_4/TiO_2$ NRs. **c** Cross-sectional SEM image of $BiVO_4/TiO_2$ NRs. **d** LSV for TiO_2 NRs and $BiVO_4/TiO_2$ NRs in 0.5M K–Pi buffer with 1M Na_2SO_3. **e** Electrochemical impedance spectra (EIS) of TiO_2 NRs and $BiVO_4/TiO_2$ NRs at 1.23 V (vs. RHE) in 0.5M K– Pi buffer with 1M Na_2SO_3. Inset shows equivalent circuit. **f** Charge injection efficiency of TiO_2 NRs and $BiVO_4/TiO_2$ NRs

 https://doi.org/10.1007/s40820-022-00795-8

Fig. S9 also showed conformally decorated $BiVO_4$ on TiO_2 NFs. Through the TEM equipped with EDS, we confirmed the detailed surface morphologies and elemental distributions of $BiVO_4/TiO_2$ NFs. The TEM image in NFs region (Fig. 3e) also indicated that $BiVO_4$ nanodots conformally covered on the surface of the TiO_2 NFs. The inset shows an enlarged TEM image of $BiVO_4$ nanodots. As shown in EDS mappings (Fig. 3f–k), all the constituent elements were well represented. High-resolution TEM (HR-TEM) images and a fast Fourier transform (FFT) pattern are shown in Fig. 3l–o. According to high-resolution TEM (HR-TEM) images and fast Fourier transform (FFT) patterns, electron diffraction patterns of the selected area showed *d*-spacing of 0.309 and 0.312 nm (Fig. 3l), corresponding to the (− 112) and (103) planes of monoclinic $BiVO_4$, respectively (Fig. 3n), and *d*-spacing of 0.29 and 0.32 nm (Fig. 3m), which can be assigned to the (001) and (110) planes of rutile TiO_2 NFs, respectively (Fig. 3o). These results are well-matched with the XRD analysis (Fig. S10).

PEC measurements of the $BiVO_4/TiO_2$ NFs with different coverages of $BiVO_4$ were performed using a standard three-electrode cell with an electrolyte of 0.5M potassium phosphate ($K–P_i$) buffer and 1M sodium sulfite (Na_2SO_3) at a scan rate of 10 mV s^{-1} under a AM 1.5G solar light. Oxidation of sulfite (SO_3^{2-}/SO_3^{-}, $E^\circ = 0.73$ V vs. NHE; $SO_3^{2\neg}/S_2O_6^{2\neg}$, $E^\circ = 0.026$ V vs. NHE), is thermodynamically and kinetically much more favorable than water oxidation [32]. Therefore, surface recombination losses due to slow interfacial hole transfer kinetics can be assumed to be negligible for the photo-oxidation of sulfite. $BiVO_4/TiO_2$ NFs were fabricated by adjusting the electrodeposition cycles of $BiVO_4$ from 0 to 36 (i.e., n $BiVO_4$ = n cycles electrodeposited $BiVO_4$), and

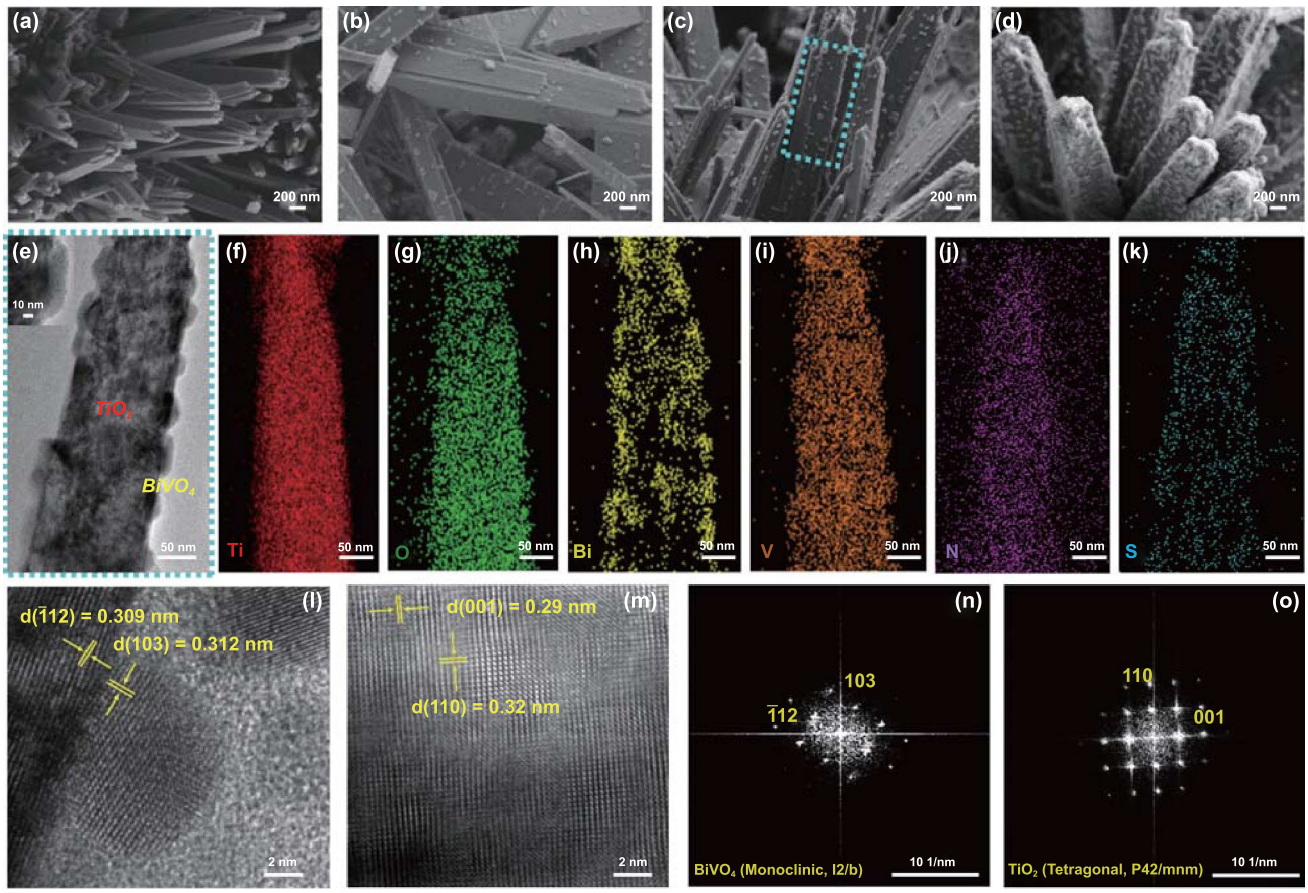

Fig. 3 SEM images of **a** TiO_2 NFs and $BiVO_4/TiO_2$ NFs with different deposition cycles of $BiVO_4$: **b** 6 cycles, **c** 18 cycles, and **d** 36 cycles. **e** TEM image of $BiVO_4/TiO_2$ NFs deposited by 18 cycles. Inset shows HR-TEM image of $BiVO_4/TiO_2$ NFs. EDS mapping images of **f** Ti, **g** O, **h** Bi, **i** V, **j** N, and **k** S. **l** Crystalline planes of (− 112) and (103) of $BiVO_4$, **m** Crystalline planes of (001) and (110) of TiO_2 NFs. FFT patterns of **n** $BiVO_4$ and **o** TiO_2 NFs

their LSV curves were recorded under the chopped (on/off) light condition. As shown in Fig. 4a, the photocurrent densities of the $BiVO_4/TiO_2$ NFs gradually increase until the number of electrodeposition cycles increases to 18 cycles and then starts to decrease. As the increase in the deposition cycle of $BiVO_4$, the density of $BiVO_4$ nanodots covering the TiO_2 NFs increases (Fig. S8b–d), adding the charge transfer sites. However, after the optimized cycles (18 cycles), the agglomeration of $BiVO_4$ nanodots is observed at the tip of TiO_2 NFs (Fig. S8e–f), interfering with the charge transfer. The highest photocurrent density of 1.7 mA cm^{-2} was obtained at 1.23 V versus RHE for the 18 $BiVO_4/TiO_2$ NFs. This value corresponds to 4.7 and 4.8 times that of the TiO_2 NFs and $BiVO_4/TiO_2$ NRs, respectively. In addition to the enlarged absorption wavelength range from the ultraviolet (UV) to ultraviolet–visible (UV–Vis) region), improved charge separation is decisive for the cause of PEC performances of $BiVO_4/TiO_2$ NFs. The electron–hole recombination is structurally reduced because the conformally coated $BiVO_4$ nanodots on TiO_2 NFs enlarge the depletion layer and shorten the charge diffusion length to the interface [14, 33]. The small size of the $BiVO_4$ nanodots allows for a high collection efficiency of electrons by the TiO_2 NFs, and the proximity of the semiconductor liquid junction allows holes to reach the surface to perform the water splitting reaction [1, 14, 33, 34]. However, after the optimal deposition cycle, increasing the surface area also has negative effects such as the formation of surface defects and grain boundaries, which degrade PEC performances. In this respect, the design of photoanodes with appropriate active areas is crucial for photoactivity [5, 35, 36].

The PEC water splitting efficiency of photoelectrodes was also quantitatively evaluated using the applied bias photon-to-current conversion efficiency (ABPE) as follows:

$$\text{ABPE}\ (\%) = J_{\text{ph}}\left(1.23 - V_{\text{b}}\right) * 100/P_{\text{total}} \quad (1)$$

where V_{b} is the applied bias (vs. RHE), J_{ph} is the photocurrent density at the measured potential, and P_{total} is the power density of light. The ABPE takes applied potential into account as important factor in the conversion of solar to chemical energy [37]. As shown in Fig. 4c, maximum photoconversion efficiency of 0.65% was achieved for the 18 $BiVO_4/TiO_2$ NFs at 0.61 V versus RHE, which was 8.1

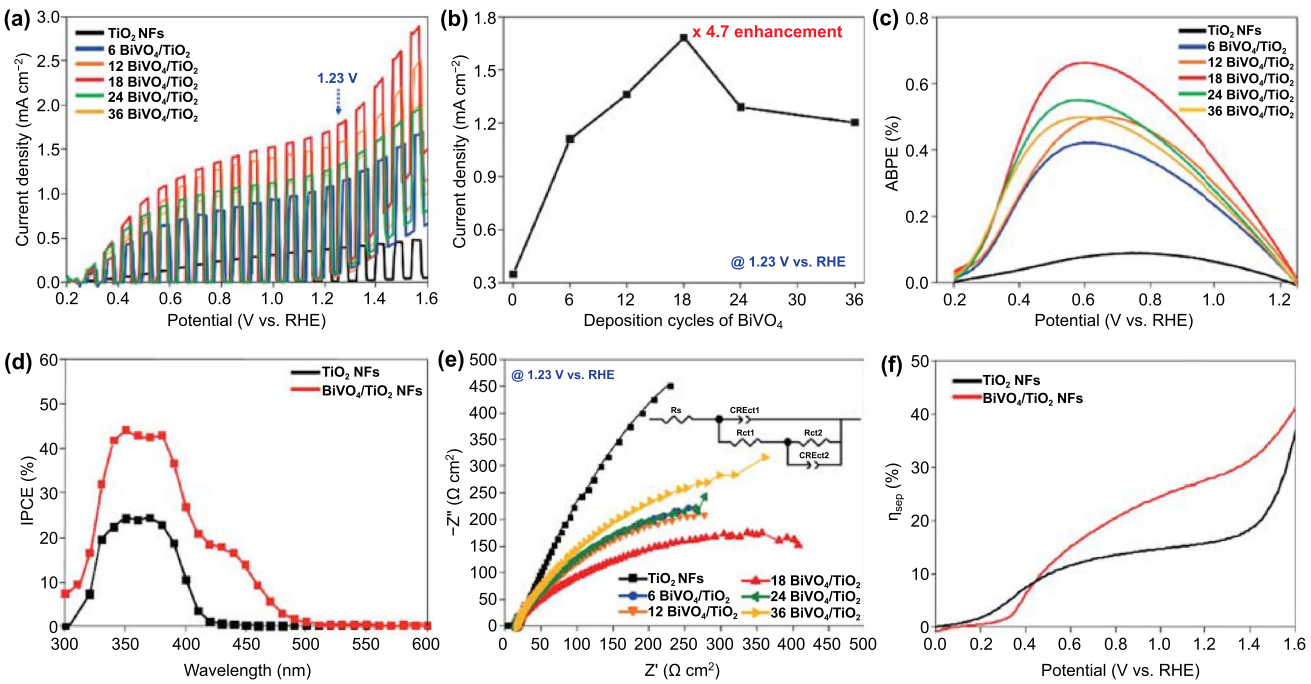

Fig. 4 **a** LSV of TiO_2 NFs and $BiVO_4/TiO_2$ NFs with different deposition cycles of $BiVO_4$ in 0.5M K–P_i buffer with 1M Na_2SO_3. **b** Photocurrent density of $BiVO_4/TiO_2$ NFs with different deposition cycles of $BiVO_4$ at 1.23 V (vs. RHE). **c** ABPE of TiO_2 NFs and $BiVO_4/TiO_2$ NFs with different deposition cycles of $BiVO_4$. **d** IPCE at 1.23 V (vs. RHE) of TiO_2 NFs and 18 $BiVO_4/TiO_2$ NFs. **e** EIS of TiO_2 NFs and $BiVO_4/TiO_2$ NFs with different deposition cycles of $BiVO_4$ at 1.23 V (vs. RHE) in 0.5M K–P_i buffer with 1M Na_2SO_3. Inset shows equivalent circuit. **f** Charge separation efficiency of TiO_2 NFs and 18 $BiVO_4/TiO_2$ NFs

https://doi.org/10.1007/s40820-022-00795-8

times higher than that of the pristine TiO_2 NFs. Also, the maximum photoconversion efficiencies for all $BiVO_4/TiO_2$ NFs were obtained at a lower applied potential than the pristine TiO_2 NFs. These are associated with the reduction of the hole injection barrier at the interface between the TiO_2 NFs and electrolyte by introduction of the $BiVO_4$ nanodots [36]. According to the IPCE spectra (Fig. 4d), the absorption wavelength edge was expanded from 430 (UV region) to 512 nm (UV–Vis region) after the introduction of $BiVO_4$. It also led to a 44% enlargement of maximum IPCE at a wavelength of 350 nm. In the chronoamperometry at 1.23 V versus RHE under 1 sun illumination, the 18 $BiVO_4/TiO_2$ NFs showed stable PEC performances for 6 h, as shown in Fig. S8h.

We also analyzed the EIS to figure out the charge transfer kinetics of $BiVO_4/TiO_2$ NFs, and the measured data were fitted to the equivalent circuit, as shown in Fig. 4e [23]. Unlike $BiVO_4/TiO_2$ NRs, the charge transfer resistance of all $BiVO_4/TiO_2$ NFs was drastically decreased compared to pristine TiO_2 NFs. These results represent the effective charge transfer at the interfaces of each semiconductor and the semiconductor/electrolyte by suppressing the charge recombination. Of these, the lowest value of charge transfer resistances ($R_{ct1} = 0.84\ \Omega\ cm^{-2}$ and $R_{ct2} = 475.11\ \Omega\ cm^{-2}$) were recorded for the 18 $BiVO_4/TiO_2$ NFs, which well corresponds to the tendency of photocurrent density (Fig. 4b).

To gain more insight into the crystal facet effect, we investigated the electronic characteristics using Mott–Schottky (M-S) analysis to grasp a flat band potential by using Eq. (2):

$$C^{-2} = \left(2/e\varepsilon\varepsilon_0 N_d\right)\left[V - V_{FB} - k_B T/e\right] \quad (2)$$

where C is the capacitance of the space charge layer, e is the electron charge ($1.602\ 10^{-19}$ C), ε is the dielectric constant, ε_0 is the permittivity of vacuum ($8.854\ 10^{-12}$ F m^{-1}), V (vs. RHE) is the applied potential, V_{FB} (vs. RHE) is the flat band potential, k_B is the Boltzmann constant ($1.381\ 10^{-23}$ J K^{-1}), T is the temperature (298 K), E is the applied potential, and N_d is the charge carrier (donor) density. The flat band potentials were determined from the intercepts of the $1/C^2$ versus V curve, subtracting $k_B T/e = 0.025$ V from the intercept. And the carrier concentration can be calculated from the slope of the M-S curves. As the slope of the M-S plot flattens, the carrier concentration increases. The flat band potential of the TiO_2 NFs is more cathodically shifted about 100 mV than the TiO_2 NRs, as shown in Fig. S11. It is favorable for the electrons to pass through the circuit to the counter electrode [5]. We analyzed the M-S plot after electrodeposition of $BiVO_4$ onto the TiO_2 NFs and TiO_2 NRs. As shown in Fig. S11a, the donor density of $BiVO_4/TiO_2$ NFs was increased, which means the internal resistance of $BiVO_4/TiO_2$ NFs is reduced, allowing the carrier to transport much faster than the pristine TiO_2 NFs. On the other hand, as shown in Fig. S11b, the carrier concentration of the $BiVO_4/TiO_2$ NRs was drastically reduced, which derives the decrease in photoactivity. These results indicate that the facet and morphology control of the bottom layer could be a significant factor in controlling PEC water splitting kinetics.

We also measured charge separation efficiency (η_{sep}) in the potential from 0 V to 1.6 V versus RHE. As shown in Fig. 4e, the $BiVO_4/TiO_2$ NFs exhibited 2.5 times higher η_{sep} than the pristine TiO_2 NFs at 1.23 V versus RHE. It directly reveals that the enhanced photocurrent density of $BiVO_4/TiO_2$ NFs was mainly originated from the improved charge separation between $BiVO_4$ nanodots and TiO_2 NFs. To support this result, we also measured PEC water oxidation performances of TiO_2 NFs and 18 $BiVO_4/TiO_2$ NFs in 0.5M K– P_i buffer without hole scavenger. As shown in Fig. S12a, $BiVO_4/TiO_2$ NFs showed more efficient water oxidation and higher photocurrent density compared to TiO_2 NFs at 1.23 V versus RHE. The lower photocurrent density of $BiVO_4/TiO_2$ NFs in the lower potential region than that of TiO_2 NFs was derived from the sluggish hole transfer of $BiVO_4$. To expedite the hole transfer at the low potential, an additional introduction of oxygen evolution catalyst to $BiVO_4$ is necessary [13]. Also, $BiVO_4/TiO_2$ NFs showed a 29% higher maximum IPCE and wider absorption wavelength range than TiO_2 NFs as shown in Fig. S12b. We also measured the EIS of TiO_2 NFs and 18 $BiVO_4/TiO_2$ NFs at 1.23 V versus RHE in K–Pi buffer electrolyte. As shown in Fig. S12c, $BiVO_4/TiO_2$ NFs showed a smaller semicircle compared to TiO_2 NFs, which represented the smaller charge transfer resistance during the water oxidation. In the chronoamperometry at 1.23 V versus RHE in K–Pi buffer electrolyte, the 18 $BiVO_4/TiO_2$ NFs showed stable PEC performances for 2 h, as shown in Fig. S12d. By using gas chromatography, we measured gas evolution and Faradaic efficiency of 18 $BiVO_4/TiO_2$ NFs at 1.23 V versus RHE. As shown in Fig. S12e, the 18 $BiVO_4/TiO_2$ NFs photoanode and Pt cathode continuously generated oxygen and hydrogen gas. Near-complete Faradaic efficiency was achieved, representing that the photogenerated charge carriers were mostly used for evolving the oxygen and hydrogen gases.

3.4 Studies of Charge Carrier Dynamics and Band Structures

To profoundly understand the effect in the crystal facet of TiO_2 nanostructures to the charge transport and recombination behavior, the transient photocurrent decay occurring immediately upon illumination was evaluated. As shown in the chronoamperometry at 1.23 V versus RHE (Fig. 5a), when the light was switched on, a photocurrent spike was observed due to the rapid generation of electron and hole pairs. It would lead to severe charge recombination and cause the decrease in the photoactivity for the water splitting reaction. In general, the charge recombination can be caused by the accumulation of either electrons in the bulk or holes at the surface. The accumulation of holes would cause an equally large cathodic transient when the light is switched off, and electrons in the conduction band react with the accumulated hole. However, cathodic transients can scarcely be observed in Fig. 5a, suggesting the accumulation of holes at the surface of the films is not the main recombination process in both $BiVO_4/TiO_2$ NFs and $BiVO_4/TiO_2$ NRs. Thus, it is represent that the transient decays were mainly dependent to the accumulation of electrons due to the poor electron transport in the photoanodes. The transient decay time in the photoanodes was calculated from the logarithmic plot of parameter D, given by Eq. (3):

$$D = \left(I_t - I_s\right)/\left(I_m - I_s\right) \tag{3}$$

where I_m is the photocurrent spike, I_t is the photocurrent at time t, and I_s is the steady-state photocurrent (i.e., as the recombination and charge generation reaches equilibrium). The transient decay time is defined as the time at which in $\ln D = -1$. Based on the photocurrent profiles measured in Fig. 5a, the transient decay time of the TiO_2 NFs, $BiVO_4/TiO_2$ NFs, TiO_2 NRs, and $BiVO_4/TiO_2$ NRs is displayed in Fig. 5b. As shown in Table S2, the transient decay time for the $BiVO_4/TiO_2$ NFs was 26.35 s, which is approximately 4.15 times longer than that of the TiO_2 NFs at about 6.36 s. It represents a lower charge recombination rate of $BiVO_4/TiO_2$ NFs compared to the TiO_2 NFs. Otherwise, the $BiVO_4/TiO_2$ NRs showed a decay time of 1.57 s, which is shorter than that of the TiO_2 NRs at about 2.58 s. It is also related to the poor charge separation between $BiVO_4$ nanodots and TiO_2 NRs. These results indicate that TiO_2 NFs can play a key role as a hole blocking layer, which expedites electron transport and reduces charge recombination.

To gain a deeper insight into charge recombination behaviors according to the TiO_2 facet, time-resolved photoluminescence (TRPL) analysis was carried out at a wavelength of 540 nm, as shown in Fig. 5c. TRPL is a powerful technique to gain information about dynamics of the photogenerated electron and hole pairs, reflecting the charge recombination/separation behavior and charge trapping process in defects [38–40]. The TRPL results were fitted with a biexponential decay function, and photoluminescence lifetimes were calculated as represented in Table S3. The nonradiative (τ_1) and radiative recombination lifetimes (τ_2) of the photoexcited electrons and holes can be determined by measuring the luminescence signals resulting from recombination [38, 40]. The nonradiative recombination lifetime is generally determined from the surface recombination by the trap sites. Since, in both heterostructured photoelectrodes, it is the same $BiVO_4$ that is the part in contact with the electrolyte on the band structures, they have similar τ_1 values. However, the electron injection behavior into adjacent layers can be investigated by monitoring the radiative recombination lifetime. If the photoexcited carriers can be effectively transported

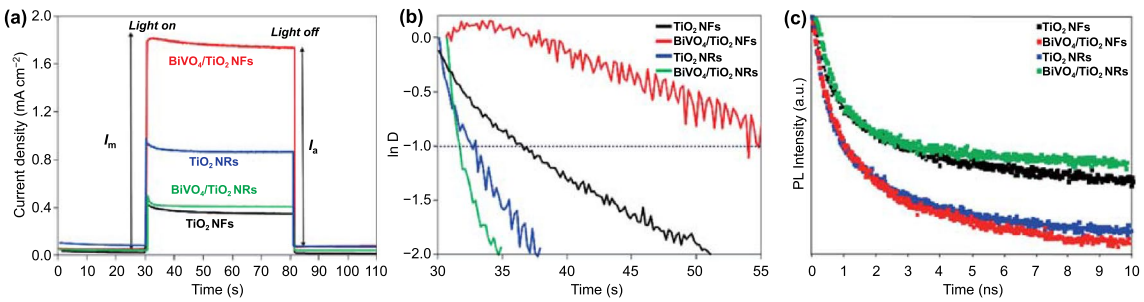

Fig. 5 **a** The transient photocurrent decay that occurs immediately upon illumination at 1.23 V (vs. RHE). **b** Transient decay times for TiO_2 NFs, TiO_2 NRs, $BiVO_4/TiO_2$ NFs, and $BiVO_4/TiO_2$ NRs. **c** TRPL of TiO_2 NFs, TiO_2 NRs, $BiVO_4/TiO_2$ NFs and $BiVO_4/TiO_2$ NRs

https://doi.org/10.1007/s40820-022-00795-8

into the neighboring layers, the radiative recombination lifetime of the heterostructured photoelectrode decreases. In this regard, the smaller τ_2 value of $BiVO_4/TiO_2$ NFs (5.20 ns) than that of $BiVO_4/TiO_2$ NRs (6.10 ns) denotes the efficient extraction of photoexcited electrons by TiO_2 NFs. It corresponds with the transient decay time analysis in Fig. 5b. Based on the analysis of charge carrier dynamics, we demonstrated that the crystal facet engineering of TiO_2 nanostructures is a powerful tool to allow TiO_2 to be utilized as the hole blocking layer for $BiVO_4$ by boosting charge separation efficiency.

To investigate the reason for the charge separation difference of TiO_2 NRs with (001) facets and TiO_2 NFs with (110) facets, we compared the band structures of $BiVO_4/TiO_2$ NRs and $BiVO_4/TiO_2$ NFs. The UPS measures occupied electronic states, providing information on the Fermi level and valence band maximum (VBM) energy of a material. The conduction band minimum (CBM) energy can be calculated by adding the optical band gap energy (E_g), which is given by the UV–Vis spectroscopy, to the VBM. The band gap can be evaluated from Eq. (4):

$$\alpha(h\nu) = A\left(h\nu - E_g\right)^{n/2} \tag{4}$$

where α, E_g, and A are the absorption coefficient, band gap energy, and a constant, respectively. Based on the UV–Vis spectra (Fig. S13) and Tauc plots, the optical band gap of the TiO_2 NFs and TiO_2 NRs was 2.84 and 2.75 eV, respectively (Fig. 6a). These are the smaller values than the band gap in previous reports (~ 3.2 eV). Because co-doped sulfur and nitrogen from the sulfamic acid form S 3p and N 2p state between the conduction band and valence band of TiO_2, diminishing the band gap of TiO_2 nanostructures [18]. And, a smaller band gap of TiO_2 NRs compared to that of TiO_2 NFs caused the absorption of the larger wavelength of visible light. Thus, as shown in Fig. 5a, the TiO_2 NRs generated a higher photocurrent density at 1.23 V versus RHE than TiO_2 NFs. According to Fig. 6b, the band gap of $BiVO_4$ was 2.4 eV, which is similar to the values in previous studies.

The secondary electron emission (SEE) spectra of the TiO_2 NFs, TiO_2 NRs, $BiVO_4$, $BiVO_4/TiO_2$ NFs, and $BiVO_4/TiO_2$ NRs were given by the high-binding-energy region in UPS, as shown in Fig. 6c. The work functions of TiO_2 NFs (4.46 eV), TiO_2 NRs (3.58 eV), $BiVO_4/TiO_2$ NFs (4.18 eV), and $BiVO_4/TiO_2$ NRs (4.18 eV) could be estimated from the differences between SEE spectra cutoffs and He I photon source energy (21.22 eV), as shown in Fig. S14. According to the valence band (VB) spectra given by the low-binding-energy region in UPS, the energy difference between the Fermi level and the valence band maximum (E_F–E_{VBM}) could be calculated, as shown in Fig. 6d. The values of E_F–E_{VBM} for the TiO_2 NFs (2.62 eV), TiO_2 NRs (2.67 eV), $BiVO_4/TiO_2$ NFs (2.39 eV), and $BiVO_4/TiO_2$ NRs (2.39 eV) were calculated by the VB spectra cutoffs, as shown in Fig. S15. The values measured by UPS are summarized in Table S4. Since the band edge positions are highly dependent on the change of electrostatic potential in near-surface atoms, the VBM and CBM shifts between TiO_2 NRs and TiO_2 NFs is derived from the preferential crystal facet [41–43]. The titanium atoms on the (001) surface are tetrahedral-coordinated, and thus their environment is relatively close to the bulk. It causes the splitting of the occupied and unoccupied levels to be large, which leads to the highest CBM value [36, 37, 41]. Therefore, the (110) facet-dominant TiO_2 NFs have a more negative CBM than the (001) facet-dominant TiO_2 NRs. Based on these results, the energy band diagrams for the $BiVO_4/TiO_2$ NRs and $BiVO_4/TiO_2$ NFs are illustrated in Fig. 6e, f, respectively. In the case of $BiVO_4/TiO_2$ NRs, the CBM of the TiO_2 NRs significantly move upward, making the transport of photogenerated electrons from $BiVO_4$ difficult [38, 40, 44, 45]. Also, due to the relatively positive VBM of the TiO_2 NRs, photogenerated holes from $BiVO_4$ cannot be effectively blocked, causing the charge recombination, whereas TiO_2 NFs having a relatively negative CBM and VBM can be effective electron transport layer and hole-blocking layer for $BiVO_4$. As a result, the $BiVO_4/TiO_2$ NFs clearly form the type II band alignment, which is energetically favorable to separate the photogenerated electrons and holes from $BiVO_4$. In the final analysis, it was found that the enhanced photoactivity of $BiVO_4/TiO_2$ NFs was originated from the improvement of charge separation according to the band structure of crystal facet-engineered TiO_2.

4 Conclusions

In summary, we have demonstrated the effect of crystal facet-controlled TiO_2 nanostructures on band structures and charge separation. Two types of $BiVO_4/TiO_2$ heterostructure photoanodes having TiO_2 NRs with (001) facets and TiO_2 NFs with (110) were systematically studied to reveal the role of facets for facile PEC water splitting. We revealed that the improved photoelectrochemical

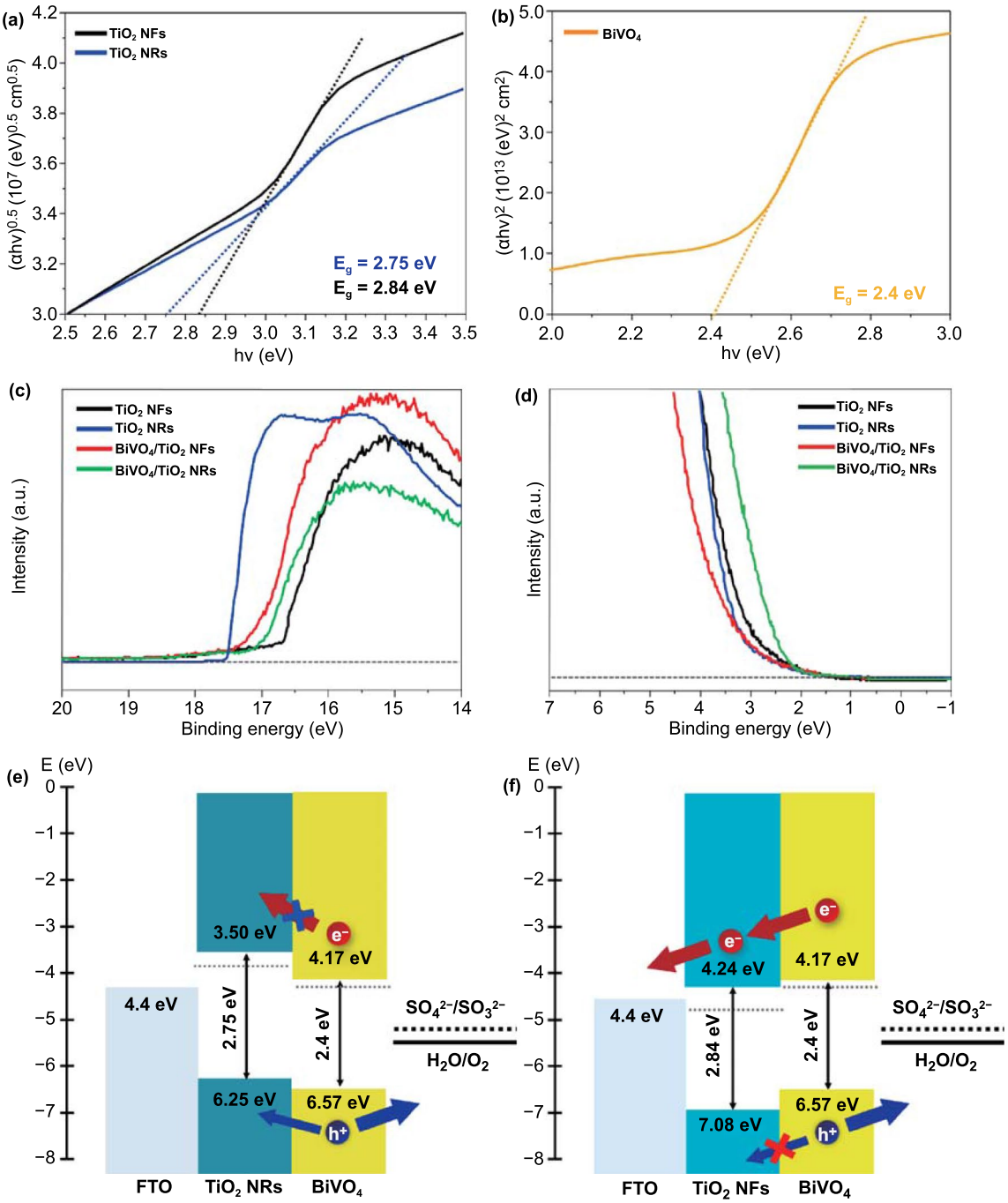

Fig. 6 UV–Vis Tauc plots of **a** TiO_2 NFs, TiO_2 NRs, and **b** $BiVO_4$. **c** Secondary electron emission spectra and **d** valence band spectra of TiO_2 NFs, TiO_2 NRs, $BiVO_4/TiO_2$ NFs, and $BiVO_4/TiO_2$ NRs. Flat band structures of **e** $BiVO_4/TiO_2$ NRs and **f** $BiVO_4/TiO_2$ NFs

performances of $BiVO_4/TiO_2$ NFs compared with $BiVO_4/TiO_2$ NRs were attributed to the prohibition of charge recombination through interface and morphology control. According to the analysis of charge carrier dynamics such as transient decay time and time-resolved photoluminescence, the charge separation effect was supported. Based on the UPS, it was represented that crystal facet engineering affects the band edge position of TiO_2. In conclusion, this study not only provides new perspectives in band structure engineering but also opens a promising

https://doi.org/10.1007/s40820-022-00795-8

avenue in designing heterostructure photoelectrodes for efficient PEC water splitting.

Acknowledgements This research was supported by the Basic Science Research Program through the National Research Foundation of Korea (NRF) funded by the Ministry of Science and ICT (MSIT) (2021R1A2B5B03001851). This work was also supported by the NRF Grant funded by the Korean government MSIT (2021M3H4A1A03057403). M. G. L. acknowledges the Basic Science Research Program through the NRF funded by the Ministry of Education (2021R1A6A3A03039988). J. W. Y. acknowledges the Basic Science Research Program through the NRF funded by the Ministry of Education (2021R1A6A3A13046700). The Inter-University Semiconductor Research Center and Institute of Engineering Research at Seoul National University provided research facilities for this work.

Funding Open access funding provided by Shanghai Jiao Tong University.

Supplementary Information The online version contains supplementary material available at https://doi.org/10.1007/s40820-022-00795-8.

References

1. C. Jiang, S.J.A. Moniz, A. Wang, T. Zhang, J. Tang, Photoelectrochemical devices for solar water splitting-materials and challenges. Chem. Soc. Rev. **46**, 4645–4660 (2017). https://doi.org/10.1039/c6cs00306k
2. I.S. Cho, Z. Chen, A.J. Forman, D.R. Kim, P.M. Rao et al., Branched TiO_2 nanorods for photoelectrochemical hydrogen production. Nano Lett. **11**, 4978–4984 (2011). https://doi.org/10.1021/nl2029392
3. J.W. Yang, S.H. Ahn, H.W. Jang, Crucial role of heterostructures in highly advanced water splitting photoelectrodes. Curr. Opin. Green Sustain. Chem. **29**, 100454 (2021). https://doi.org/10.1016/j.cogsc.2021.100454
4. K. Sivula, F. le Formal, M. Grätzel, WO_3-Fe_2O_3 photoanodes for water splitting: a host scaffold, guest absorber approach. Chem. Mater. **21**, 2862–2867 (2009). https://doi.org/10.1021/cm900565a
5. M.G. Lee, D.H. Kim, W. Sohn, C.W. Moon, H. Park et al., Conformally coated $BiVO_4$ nanodots on porosity-controlled WO_3 nanorods as highly efficient type II heterojunction photoanodes for water oxidation. Nano Energy **28**, 250–260 (2016). https://doi.org/10.1016/j.nanoen.2016.08.046
6. J. Su, L. Guo, N. Bao, C.A. Grimes, Nanostructured WO_3/$BiVO_4$ heterojunction films for efficient photoelectrochemical water splitting. Nano Lett. **11**, 1928–1933 (2011). https://doi.org/10.1021/nl2000743
7. X. Shi, I.Y. Choi, K. Zhang, J. Kwon, D.Y. Kim et al., Efficient photoelectrochemical hydrogen production from bismuth vanadate-decorated tungsten trioxide helix nanostructures. Nat. Commun. **5**, 4775 (2014). https://doi.org/10.1038/ncomms5775
8. A. Kargar, S.J. Kim, P. Allameh, C. Choi, N. Park et al., p-Si/SnO_2/Fe_2O_3 Core/Shell/Shell nanowire photocathodes for neutral pH water splitting. Adv. Funct. Mater. **25**, 2609–2615 (2015). https://doi.org/10.1002/adfm.201404571
9. L. Wang, A. Palacios-Padrós, R. Kirchgeorg, A. Tighineanu, P. Schmuki, Enhanced photoelectrochemical water splitting efficiency of a hematite-ordered Sb:SnO_2 host-guest system. Chemsuschem **7**, 421–424 (2014). https://doi.org/10.1002/cssc.201301120
10. S. Shen, S.A. Lindley, X. Chen, J.Z. Zhang, Hematite heterostructures for photoelectrochemical water splitting: Rational materials design and charge carrier dynamics. Energy Environ. Sci. **9**, 2744–2775 (2016). https://doi.org/10.1039/c6ee01845a
11. B.R. Lee, H.W. Jang, β-In_2S_3 as water splitting photoanodes: promise and challenges. Electron. Mater. Lett. **17**, 119–135 (2021). https://doi.org/10.1007/s13391-020-00266-5
12. S. Byun, B. Kim, S. Jeon, B. Shin, Effects of a SnO_2 hole blocking layer in a $BiVO_4$-based photoanode on photoelectrocatalytic water oxidation. J. Mater. Chem. A **5**, 6905–6913 (2017). https://doi.org/10.1039/c7ta00806f
13. J.W. Yang, I.J. Park, S.A. Lee, M.G. Lee, T.H. Lee et al., Near-complete charge separation in tailored $BiVO_4$-based heterostructure photoanodes toward artificial leaf. Appl. Catal. B: Environ. **293**, 120217 (2021). https://doi.org/10.1016/j.apcatb.2021.120217
14. J. Resasco, H. Zhang, N. Kornienko, N. Becknell, H. Lee et al., TiO_2/$BiVO_4$ nanowire heterostructure photoanodes based on type II band alignment. ACS Cen. Sci. **2**, 80–88 (2016). https://doi.org/10.1021/acscentsci.5b00402
15. Z. Yu, H. Liu, M. Zhu, Y. Li, W. Li, Interfacial charge transport in 1D TiO_2 based photoelectrodes for photoelectrochemical water splitting. Small **17**, 1903378 (2021). https://doi.org/10.1002/smll.201903378
16. O. Monfort, D. Raptis, L. Satrapinskyy, T. Roch, G. Plesch et al., Production of hydrogen by water splitting in a photoelectrochemical cell using a $BiVO_4$/TiO_2 layered photoanode. Electrochim. Acta **251**, 244–249 (2017). https://doi.org/10.1016/j.electacta.2017.08.125

17. X. Zhang, B. Zhang, K. Cao, J. Brillet, J. Chen et al., A perovskite solar cell-TiO_2@$BiVO_4$ photoelectrochemical system for direct solar water splitting. J. Mater. Chem. A **3**, 21630–21636 (2015). https://doi.org/10.1039/c5ta05838d
18. D.M. Andoshe, K. Yim, W. Sohn, C. Kim, T.L. Kim et al., One-pot synthesis of sulfur and nitrogen codoped titanium dioxide nanorod arrays for superior photoelectrochemical water oxidation. Appl. Catal. B: Environ. **234**, 213–222 (2018). https://doi.org/10.1016/j.apcatb.2018.04.045
19. S. Wang, G. Liu, L. Wang, Crystal facet engineering of photoelectrodes for photoelectrochemical water splitting. Chem. Rev. **119**, 5192–5247 (2019). https://doi.org/10.1021/acs.chemrev.8b00584
20. B. Fu, Z. Wu, S. Cao, K. Guo, L. Piao, Effect of aspect ratios of rutile TiO_2 nanorods on overall photocatalytic water splitting performance. Nanoscale **12**, 4895–4902 (2020). https://doi.org/10.1039/c9nr10870j
21. C. Phawa, S. Prayoonpokarach, K. Sinthiptharakoon, P. Chakthranont, W. Sangkhun et al., Effects of matching facet pairs of TiO_2 on photoelectrochemical water splitting behaviors. ChemCatChem **12**, 2116–2124 (2020). https://doi.org/10.1002/cctc.201901857
22. L. Wang, J. Ge, A. Wang, M. Deng, X. Wang et al., Designing p-type semiconductor-metal hybrid structures for improved photocatalysis. Angew. Chem. **126**, 5207–5211 (2014). https://doi.org/10.1002/ange.201310635
23. M.G. Lee, K. Jin, K.C. Kwon, W. Sohn, H. Park et al., Efficient water splitting cascade photoanodes with ligand-engineered MnO cocatalysts. Adv. Sci. **5**, 1800727 (2018). https://doi.org/10.1002/advs.201800727
24. J.P. Jalava, V.M. Taavitsainen, R.J. Lamminmäki, M. Lindholm, S. Auvinen et al., Modeling TiO_2's refractive index function from bulk to nanoparticles. J. Quant. Spec. Radiat. Transf. **167**, 105–118 (2015). https://doi.org/10.1016/j.jqsrt.2015.08.007
25. J.M. Ball, S.D. Stranks, M.T. Hörantner, S. Hüttner, W. Zhang et al., Optical properties and limiting photocurrent of thin-film perovskite solar cells. Energy Environ. Sci. **8**, 602–609 (2015). https://doi.org/10.1039/c4ee03224a
26. S.S.M. Bhat, S.A. Lee, T.H. Lee, C. Kim, J. Park et al., All-solution-processed $BiVO_4$/TiO_2 photoanode with $NiCo_2O_4$ nanofiber cocatalyst for enhanced solar water oxidation. ACS Appl. Energy Mater. **3**, 5646–5656 (2020). https://doi.org/10.1021/acsaem.0c00607
27. S.P. Hong, J. Park, S.S.M. Bhat, T.H. Lee, S.A. Lee et al., Comprehensive study on the morphology control of TiO_2 nanorods on foreign substrates by the hydrothermal method. Cryst. Growth Des. **18**, 6504–6512 (2018). https://doi.org/10.1021/acs.cgd.8b00609
28. S.S. Mali, C.A. Betty, P.N. Bhosale, P.S. Patil, C.K. Hong, From nanocorals to nanorods to nanoflowers nanoarchitecture for efficient dye-sensitized solar cells at relatively low film thickness: all hydrothermal process. Sci. Rep. **4**, 5451 (2014). https://doi.org/10.1038/srep05451
29. J. Harris, R. Silk, M. Smith, Y. Dong, W.T. Chen et al., Hierarchical TiO_2 nanoflower photocatalysts with remarkable activity for aqueous methylene blue photo-oxidation. ACS Omega **5**, 18919–18934 (2020). https://doi.org/10.1021/acsomega.0c02142
30. M. Ge, Q. Li, C. Cao, J. Huang, S. Li et al., One-dimensional TiO_2 nanotube photocatalysts for solar water splitting. Adv. Sci. **4**, 1600152 (2017). https://doi.org/10.1002/advs.201600152
31. J.S. Yang, W.P. Liao, J.J. Wu, Morphology and interfacial energetics controls for hierarchical anatase/rutile TiO_2 nanostructured array for efficient photoelectrochemical water splitting. ACS Appl. Mater. Interfaces **5**, 7425–7431 (2013). https://doi.org/10.1021/am401746b
32. T.W. Kim, K.S. Choi, Nanoporous $BiVO_4$ photoanodes with dual-layer oxygen evolution catalysts for solar water splitting. Science **343**, 990–994 (2014). https://doi.org/10.1126/science.1246913
33. A.P. Singh, N. Kodan, B.R. Mehta, A. Held, L. Mayrhofer et al., Band edge engineering in $BiVO_4$/TiO_2 heterostructure: enhanced photoelectrochemical performance through improved charge transfer. ACS Catal. **6**, 5311–5318 (2016). https://doi.org/10.1021/acscatal.6b00956
34. S. Kment, F. Riboni, S. Pausova, L. Wang, L. Wang et al., Photoanodes based on TiO_2 and α-Fe_2O_3 for solar water splitting-superior role of 1D nanoarchitectures and of combined heterostructures. Chem. Soc. Rev. **46**, 3716–3769 (2017). https://doi.org/10.1039/c6cs00015k
35. C.X. Kronawitter, L. Vayssieres, S. Shen, L. Guo, D.A. Wheeler et al., A perspective on solar-driven water splitting with all-oxide hetero-nanostructures. Energy Environ. Sci. **4**, 3889–3899 (2011). https://doi.org/10.1039/c1ee02186a
36. F.E. Osterloh, Inorganic nanostructures for photoelectrochemical and photocatalytic water splitting. Chem. Soc. Rev. **42**, 2294–2320 (2013). https://doi.org/10.1039/c2cs35266d
37. B. Lamm, B.J. Trześniewski, H. Döscher, W.A. Smith, M. Stefik, Emerging postsynthetic improvements of $BiVO_4$ photoanodes for solar water splitting. ACS Energy Lett. **3**, 112–124 (2018). https://doi.org/10.1021/acsenergylett.7b00834
38. J.K. Kim, Y. Cho, M.J. Jeong, B. Levy-Wendt, D. Shin et al., Rapid formation of a disordered layer on monoclinic $BiVO_4$: co-catalyst-free photoelectrochemical solar water splitting. Chemsuschem **11**, 933–940 (2018). https://doi.org/10.1002/cssc.201702173
39. A. Li, X. Chang, Z. Huang, C. Li, Y. Wei et al., Thin heterojunctions and spatially separated cocatalysts to simultaneously reduce bulk and surface recombination in photocatalysts. Angew. Chem. Int. Ed. **55**, 13734–13738 (2016). https://doi.org/10.1002/anie.201605666
40. W. Yang, S. Lee, H.C. Kwon, J. Tan, H. Lee et al., Time-resolved observations of photo-generated charge-carrier dynamics in Sb_2Se_3 photocathodes for photoelectrochemical water splitting. ACS Nano **12**, 11088–11097 (2018). https://doi.org/10.1021/acsnano.8b05446
41. G. Liu, H.G. Yang, J. Pan, Y.Q. Yang, G.Q.M. Lu et al., Titanium dioxide crystals with tailored facets. Chem. Rev. **114**, 9559–9612 (2014). https://doi.org/10.1021/cr400621z

 https://doi.org/10.1007/s40820-022-00795-8

42. T.R. Esch, T. Bredow, Band positions of Rutile surfaces and the possibility of water splitting. Surf. Sci. **665**, 20–27 (2017). https://doi.org/10.1016/j.susc.2017.08.006
43. S. Selcuk, A. Selloni, Facet-dependent trapping and dynamics of excess electrons at anatase TiO_2 surfaces and aqueous interfaces. Nat. Mater. **15**, 1107–1112 (2016). https://doi.org/10.1038/nmat4672
44. A.Y. Zhang, W.Y. Wang, J.J. Chen, C. Liu, Q.X. Li et al., Epitaxial facet junctions on TiO_2 single crystals for efficient photocatalytic water splitting. Energy Environ. Sci. **11**, 1444–1448 (2018). https://doi.org/10.1039/c7ee03482b
45. L. Lin, Z. Lin, J. Zhang, X. Cai, W. Lin et al., Molecular-level insights on the reactive facet of carbon nitride single crystals photocatalysing overall water splitting. Nat. Catal. **3**, 649–655 (2020). https://doi.org/10.1038/s41929-020-0476-3